WILEY | Hindawi

Research Article

Development and Validation of an Improved Quasisteady Flow Model with Additional Parasitic Loss Effects for Stirling Engines

Dong-Jun Kim ⓘ**, Young-Chae Park** ⓘ**, and Kyuho Sim** ⓘ

Department of Mechanical System Design Engineering, Seoul National University of Science and Technology, 232 Gongneung-ro, Nowon-gu, Seoul 01811, Republic of Korea

Correspondence should be addressed to Kyuho Sim; khsim@seoultech.ac.kr

This paper presents the development and validation of an improved quasisteady flow model (iQSFM) that applies comprehensive parasitic losses to the quasisteady flow model (QSFM) considering an oscillating flow, which is the actual type of flow occurring in a regenerator. Validation of iQSFM was evaluated by comparing it with a QSFM based on the experimental results of a RE-1000 regenerator. Compared to QSFM, iQSFM improved the prediction accuracy by reducing the indicated power error from 66.7% to 24.9% and the efficiency error from 35.3% to 9.4%. In addition, the prediction accuracy of iQSFM was compared when the oscillating flow and the steady flow correlation were applied to a regenerator. When iQSFM applied an oscillating flow correlation to the regenerator, it predicted the experimental results of RE-1000 slightly more accurately than in a steady flow correlation. Finally, the engine performance and parasitic losses were analyzed through a parameter study of RE-1000 using iQSFM. Through this, it was confirmed with iQSFM that the RE-1000 is designed to maximize the engine performance by minimizing the parasitic losses.

1. Introduction

Strict environmental restrictions and rising energy demand levels have recently increased the need for ecofriendly energy and energy-efficient technologies. Worldwide research and development efforts are focusing on what is known as combined heat and power (CHP) system, which increases the total energy efficiency by producing electricity and heat at the same time by utilizing thermal energy [1, 2]. Due to its great thermal efficiency, the Stirling engine in particular has received a considerable amount of attention as a power production system for the micro-CHP system [3]. The Stirling engine is also thought to be a powerful technology that can produce electricity using a variety of renewable thermal energies with good fuel flexibility as well [2, 4, 5].

The Stirling engine was invented in 1816 by Robert Stirling [6]. The Stirling engine did not receive much attention at the time due to technical limitations and the rapid growth of the internal combustion engine. However, the reduction of highly carbon-emitting internal combustion engines and advancements in manufacturing technologies have recently

renewed interest in Stirling engines [7, 8]. In particular, the free-piston Stirling engine (FPSE) proposed by Beale replaced the crank mechanism of the existing kinematic Stirling engine with spring elements and improved the durability, leading to technological advancements in the Stirling engine [9].

The Stirling engine is a heat engine based on the Stirling cycle that converts thermal energy into kinetic energy by compressing and expanding a working gas in an enclosed space through the reciprocating motion of two pistons at different temperatures. The thermal efficiency of the Stirling cycle is theoretically identical to the Carnot thermal efficiency. However, practical Stirling engines have lower efficiency than ideal Stirling cycles due to the limited heat transfer performance and certain structural limitations. As a result, Stirling engines must be designed and optimized using a Stirling cycle-based performance analysis that considers various losses.

The Stirling cycle analysis models studied thus far are classified into five generations with empirical, analytical, and numerical methods according to Dyson [10].

First, the zeroth-generation model is an empirical model that shows a correlation between the operating conditions

and the engine performance based on extensive test data of commercial engines. William Beale was the first to develop this model, which forecasts the engine performance using the Beale number, a performance coefficient, the engine charge pressure, and the operating frequency [11]. The simplest model is used to determine the performance level quickly in the concept design stage; however, the prediction accuracy is very low.

The first-generation model was proposed by Schmidt [12] as an analytical model. The Schmidt model makes predictions of engine performance outcomes by computing the dynamic working pressure according to the piston motion using a closed-form equation based on the isothermal conditions in the working spaces. Because the isothermal process can only be achieved by infinite heat transfer, it overestimates the engine's performance by around 80–100% [13].

The second-generation model was initially proposed by Finkelstein [14] as a numerical model based on ideal adiabatic conditions. The ideal adiabatic model assumes adiabatic conditions in the expansion and compression spaces but assumes isothermal conditions in the heater, cooler, and regenerator, as in the first-generation model. Note that the processes of expansion and compression are closer to the adiabatic condition in which heat transfer with the outside barely occurs [15]. However, the ideal adiabatic model also assumes an infinite heat transfer of the heat exchanger, meaning that the engine performance is highly overestimated.

Urieli and Berchowitz [13] presented a quasisteady flow model (QSFM) that improved the accuracy of performance predictions by considering the heat transfer performance of the actual heat exchanger based on the ideal adiabatic model. QSFM utilizes practical heat transfer coefficients calculated under steady flow conditions. QSFM still predicts the engine performance as 50–70% higher because it does not account for the engine's various parasitic losses [13]. Several analytical studies take the parasitic losses into account for higher prediction accuracy rates [16–18].

The third-generation model predicts the engine performance numerically using the finite difference method (FDM). The Stirling engine's spaces are divided into a number of one-dimensional control volumes. Unlike the second-generation model, the third-generation model can calculate the velocity, temperature, density, and pressure profile of the working fluid at all points in the engine control volume. This model was studied by Finkelstein [19], Urieli et al. [20], Berchowitz and Rallis [21], and Shock [22]. Also, SAGE [23, 24], developed by Gedeon and commercialized as a representative Stirling cycle analysis program, has been used by many researchers [25, 26].

The fourth-generation model uses computational fluid dynamics (CFD) to simulate the engine in detail [27–29]. This model has the advantage of being able to obtain and visualize detailed analysis results such as the flow rate, temperature, and pressure distribution of the working gas inside the engine. However, it has the drawbacks of a long calculation time and the need to establish a new model whenever the engine is changed.

On the other hand, Jan and Marek [30] compared engine performance prediction results between the second-generation model considering the parasitic loss and the fourth-generation model. The prediction accuracy rates of the two models were similar, but the computation time of the second-generation model was significantly lower, which led to claims that its engine design and optimization were more effective. This demonstrates that the second-generation model, considering various losses, is most suitable for engine design and optimization purposes. In particular, QSFM, the most advanced model proposed by Urieli and Berchowitz among the second-generation models, is being utilized and improved by various researchers.

Parlak et al. [31] used QSFM without considering engine losses to analyze a gamma-type Stirling engine for a biomass heat source. However, they neglected to study improvements of the prediction accuracy of the model. Sowale et al. [32] improved the regenerator part of QSFM and conducted a design optimization study using the genetic algorithm of a gamma-type FPSE. They divided the regenerator space from the original two cells into ten cells to improve the prediction accuracy of the regenerator temperature in QSFM. However, this model has the limitation of not considering parasitic losses other than that caused by the heat exchanger flow friction.

Li et al. [33] developed a QSFM considering the parasitic loss for a performance analysis of a beta-type FPSE for a space reactor power system. However, this model does not consider the seal leakage loss, which is one of the most significant losses in the Stirling engine. As a result, the prediction errors of the power output reach about 40% between the analysis result and the experimental result (GPU-3 engine).

This study introduces an improved quasisteady flow model (iQSFM) that applies comprehensive parasitic losses to QSFM considering an oscillating flow, which is the actual flow occurring in a regenerator. Verification of iQSFM is conducted using the experimental results of RE-1000, a representative FPSE developed by NASA. In addition, the analysis results of iQSFM are compared for steady flows and oscillating flows in the regenerator. Finally, the engine performance and loss characteristics are examined through a parameter study of the RE-1000 using iQSFM.

2. Improved Quasi-Steady Flow Model

2.1. Model Descriptions. QSFM calculates the heat input and heat removal of the engine considering the heat transfer coefficient of the heat exchanger and the temperature difference between the wall and the working gas to reflect the performance of a nonideal heat exchanger practically. Also, with regard to parasitic losses, only the flow friction loss due to a pressure drop is considered. In QSFM, the wall temperatures of the heater and cooler are assumed to be isothermal, but the temperature of the working gas varies throughout the cycle. Given that the regenerator has a longitudinal temperature gradient, the regenerator space is generally divided into two parts. The matrix temperature of the regenerator is calculated from the law of conservation of energy. The compression and expansion spaces are assumed to be adiabatic, and thus, there is no heat input or removal. More details about QSFM are presented in the literature [13].

Here, iQSFM considers various parasitic losses comprehensively to improve the accuracy of performance predictions based on the conventional QSFM. The friction coefficient and the convective heat transfer coefficient of the regenerator were calculated under a general steady flow and a more realistic oscillating flow, and the results are compared. In addition, the regenerator is divided into ten cells in iQSFM instead of the two cells used in the existing QSFM in order to enhance the prediction accuracy of the temperature gradient in the longitudinal direction of the regenerator.

2.2. Parasitic Loss Model. iQSFM considers seven parasitic losses. The types of losses are divided into the external heat loss, the internal heat loss, and the power loss, and there are differences in the methods used to combine the model according to the type of loss.

First, the external heat loss is the heat loss that occurs when the heat supplied from the heater is not transferred to the working gas and is directly removed by the cooler. It is a type of heat conduction loss through the cylinder wall between the engine's high and low temperatures. It is added to the heat removed from the cooler and subtracted from the heat supplied by the heater. The external heat loss is not associated with the energy equation for the operating gas. Additionally, it is assumed that the radiation heat loss of the heater head is not considered.

On the other hand, the internal heat loss and power loss are calculated by directly reflecting them in the energy equation of each flow system. The internal heat loss is the heat that is lost when it escapes through the cooler without being converted into any indicated power, even when the heat supplied from the heater is transferred to the working gas. The internal heat loss consists of the reheat loss, appendix gap loss, seal leakage loss, and flow friction loss in the heat exchanger and regenerator.

The reheat loss is the heat loss caused by the difference between the heat stored in the regenerator and the heat exhausted. When the working gas moves from the heater to the cooler (hot stream), the heat stored in the regenerator matrix is released back to the working gas when the working gas moves from the cooler to the heater (cold stream). That is, reheat loss arises because the heat stored in the hot stream is not completely reheated from the regenerator matrix to the working gas in the cold stream due to the limited heat transfer between the regenerator matrix and the working gas. The seal leakage loss is caused by enthalpy leakages due to the flow across the piston seals at different temperatures [13]. Because iQSFM uses the assumption of a periodic steady state and the law of conservation of mass, the net leakage of the working gas through the seal is zero. The appendix gap refers to a wide gap at the top of the DP seal. The appendix gap loss is composed of the heat conduction loss through the DP wall and the shuttle loss that arises when transferring the heat that the DP wall receives through the high-temperature part to the low-temperature part due to the DP reciprocating motion [13, 17, 34]. The flow friction loss of the heat exchanger and regenerator is the loss caused by the pressure drop due to the flow friction between the heat exchanger wall and the working gas [13].

The power loss is the loss that occurs when the indicated power is converted to mechanical power. It consists of the seal friction loss and the gas spring hysteresis loss. The seal friction loss is the loss caused by viscous friction due to the shear stress of the gas in the seal gap. The gas spring hysteresis loss is a thermodynamic loss that occurs when the bounce space acts as a gas spring and forms a hysteresis loop between the pressure and volume when it is compressed and expanded.

The formula for the parasitic loss model is summarized in Table 1. The derivation processes for each of the loss models are described in detail in the literature [13]. They are omitted here for brevity.

2.3. Thermal Model. Figure 1 shows the iQSFM conceptual diagram for a beta-type Stirling engine. The working space is composed of five spaces: the compression space, cooler, regenerator, heater, and expansion space. In particular, the regenerator is composed of ten cells. The flow of the working gas and the displacement of the displacer piston (DP) and power piston (PP) are positives in the direction from compression space to the expansion space. iQSFM has the following main assumptions [13]:

(i) The working gas is an ideal gas

(ii) The potential energy and kinetic energy of the working gas are ignored

(iii) The mass of the working gas in the engine is constant

(iv) All flows in the engine are in a periodic steady state

(v) The motions of DP and PP are sinusoidal with a constant amplitude, phase, and frequency

(vi) The engine radial temperature distribution is neglected

iQSFM employs the ideal gas equation, $pV = mRT$, to define and analyze the gas properties in the working spaces, where p, V, m, and T are the pressure, volume, mass, and temperature of the working gas, respectively.

2.3.1. Volume Definition. First, regarding the volume of each space, the heater, regenerator, and cooler, which comprise the heat exchanger part, maintain a constant volume during the cycle processes while the expansion and compression spaces change in volume, as shown in Eqs. (1) and (2), respectively, due to the DP and PP movements.

$$V_e = V_{e0} - A_d X_d \sin \omega t, \tag{1}$$

$$V_c = V_{c0} + (A_d - A_{\mathrm{rod}})X_d \sin \omega t - A_p X_p \sin (\omega t - \alpha). \tag{2}$$

Here, V_{e0} and V_{c0} are correspondingly the initial volumes of the expansion and compression spaces when DP and PP are in their equilibrium positions. A_d, A_p, and A_{rod} are the cross-sectional areas of the DP, PP, and rod, respectively. X_d, X_p, ω, and α are the DP amplitude, PP amplitude, operating frequency, and phase difference, respectively. Note

TABLE 1: Equations of the parasitic loss model (here, $i = c, k, r1 \cdots r10, h, e$, and $j = d, p$).

| Losses		Equations
External heat losses	Structure conduction loss	$\dot{Q}_{cond} = k_{cyl} \dfrac{A_{cyl}}{L_{cyl}} (T_{wh} - T_{wk})$
Internal heat losses	Regenerator reheat loss	$\dot{Q}_{reh} = (1 - \varepsilon) h_r A_{wt,r} (T_{mr} - T_r)$
	Appendix gap loss	$\dot{Q}_{app} = \pi \dfrac{d_d}{2h_{app}} k_{gas} X_d{}^2 \dfrac{(T_e - T_c)}{L_{app}} + k_d \dfrac{A_d}{L_d} (T_e - T_c)$
	leakage loss	$\dot{Q}_{leak,j} = \dot{m}_{leak,j} c_p (T_{in.j} - T_{out.j})$
	Flow friction loss	$\dot{Q}_{hf,i} = \Delta p_i A_{fr,i} \dfrac{g_i}{\rho_i}$
Power losses	Gas spring hysteresis loss	$\dot{W}_{gsh,j} = \sqrt{\dfrac{1}{32} \omega \gamma^3 (\gamma - 1) T_{w,j} p k_{gas}} \left(\dfrac{\bar{V}_{b,j}}{V_{b,j}} \right)^2 A_{wt,j}$
	Seal friction loss	$\dot{W}_{sf,j} = -v_j \left[\dfrac{\mu L_{sl,j} \pi d_j v_j}{H_j} + \dfrac{\mu d_j h_{sl,j} \left(p_{out,j} - p_{in,j} \right)}{2} \right]$
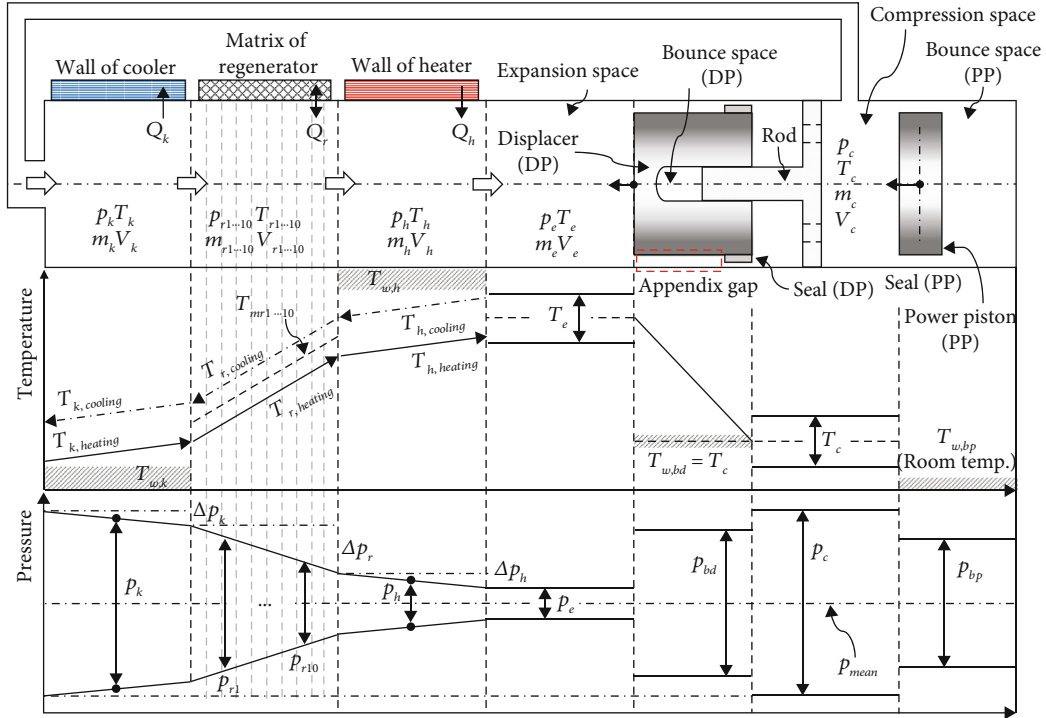
FIGURE 1: Schematic model of iQSFM and distribution of the temperature and pressure for the engine spaces.

that the expansion-space volume is a function of the DP motion only, while the compression-space volume is a function of the DP and PP motions.

2.3.2. Temperature Definition.
The temperatures to be defined in iQSFM are the heater and cooler wall temperatures, the regenerator matrix temperature, the working gas temperature in each space, and the temperature at the boundary between each space. The heater and cooler wall temperatures are assumed to be maintained isothermally. On the other hand, the heater and cooler gas temperature and the regenerator gas

temperature in each cell change during the engine cycle. The regenerator matrix temperature varies as well. The expansion and compression space temperatures are assumed to follow an adiabatic process. The temperature in all spaces is determined by the ideal gas equation of Eq. (3) with the other gas properties.

$$T_i = \frac{p_i V_i}{R m_i}, \tag{3}$$

where $i = c, k, r1 \cdots r10, h, e$.

The interface temperature of each space is determined by the temperature of the upper stream according to the flow direction of the working gas and is defined as follows:

If $\dot{m}_{ck} > 0$ then $T_{ck} \longleftarrow T_c$ otherwise $T_{ck} \longleftarrow T_k$, (4)

If $\dot{m}_{kr1} > 0$ then $T_{kr1} \longleftarrow T_k$ otherwise $T_{kr1} \longleftarrow T_{kr1}$, (5)

If $\dot{m}_{r10h} > 0$ then $T_{r10h} \longleftarrow T_{r10h}$ otherwise $T_{r10h} \longleftarrow T_h$, (6)

If $\dot{m}_{he} > 0$ then $T_{he} \longleftarrow T_h$ otherwise $T_{he} \longleftarrow T_e$. (7)

Here, the subscript ij indicates the boundary between the ith cell and the jth cell.

The temperature at the boundaries of the regenerator cells is calculated using Eqs. (8)–(10), assuming a linear distribution between the heater and cooler gas temperatures.

$$T_{kr1} = \frac{(3T_{r1} - T_{r2})}{2}, \tag{8}$$

$$T_{r1r2} = \frac{(T_{r1} + T_{r2})}{2},$$

$$\vdots \tag{9}$$

$$T_{r9r10} = \frac{(T_{r9} + T_{r10})}{2},$$

$$T_{r10h} = \frac{(3T_{r10} - T_{r9})}{2}. \tag{10}$$

The temperature of the regenerator matrix is defined by the law of conservation of energy, assuming that the amount of heat lost by the regenerator matrix is equal to the amount of heat gained by the working gas inside the regenerator cell.

$$\dot{T}_{mr1} = -\frac{\dot{Q}_{r1}}{c_{mr}},$$

$$\vdots \tag{11}$$

$$\dot{T}_{mr10} = -\frac{\dot{Q}_{r10}}{c_{mr}},$$

where c_{mr} is the heat capacity of the regenerator matrix and is constant over the cells.

2.3.3. Pressure and Mass Calculation. The pressure and mass of each space are calculated by solving the energy equation of each space with the volume and temperature defined through the above equations. The energy equation considers the heat flow, enthalpy change, work done, internal energy, and parasitic losses. The work done and internal energy can be simplified using the ideal gas equation and the relationship between the gas constant and specific heat, $R = c_p - c_v$, leading to

$$\dot{Q}_i - \dot{Q}_{\mathrm{reh},i} - \dot{Q}_{\mathrm{app}} - \dot{Q}_{\mathrm{hf}} \pm Q_{\mathrm{leak},j} + c_p(T_{\mathrm{in}}\dot{m}_{\mathrm{in}} - T_{\mathrm{out}}\dot{m}_{\mathrm{out}})$$
$$= \frac{c_v}{R}\dot{p}_i V_i + \frac{c_p}{R}p_i \dot{V}_i - \dot{W}_{\mathrm{gsh},j} - \dot{W}_{\mathrm{sf},j}, \tag{12}$$

where $i = c, k, r1 \cdots r10, h, e, \; j = d, p$.

Based on Eq. (12), the energy equations for the working gas in the compression space, cooler, regenerator, heater, and expansion space are expressed as follows:

$$\text{Compression}: \dot{Q}_{\mathrm{leak},d} + \dot{Q}_{\mathrm{leak},p} - c_p\dot{m}_{ck}T_{ck} = \frac{c_v}{R}(\dot{p}_c V_c) + \frac{c_p}{R}(p_c \dot{V}_c) - \dot{W}_{\mathrm{gsh},p} - \dot{W}_{\mathrm{sf},p}, \tag{13}$$

$$\text{Cooler}: \dot{Q}_k - \dot{Q}_{\mathrm{hf},k} + c_p(\dot{m}_{ck}T_{ck} - \dot{m}_{kr1}T_{kr1}) = \frac{c_v}{R}(\dot{p}_k V_k), \tag{14}$$

$$\dot{Q}_{r1} - \dot{Q}_{\mathrm{reh1}} - \dot{Q}_{\mathrm{hf},r1} + c_p(\dot{m}_{kr1}T_{kr1} - \dot{m}_{r1,r2}T_{r1,r2}) = \frac{c_v}{R}(\dot{p}_{r1}V_{r1}),$$

$$\text{Regenerator}: \qquad\qquad\qquad\qquad \vdots \tag{15}$$

$$\dot{Q}_{r10} - \dot{Q}_{\mathrm{reh},10} - \dot{Q}_{\mathrm{hf},r10} + c_p(\dot{m}_{r9,r10}T_{r9,r10} - \dot{m}_{r10,h}T_{r10,h}) = \frac{c_v}{R}(\dot{p}_{r10}V_{r10}),$$

$$\text{Heater}: \dot{Q}_h - \dot{Q}_{\mathrm{hf},h} + c_p(\dot{m}_{r10,h}T_{r10,h} - \dot{m}_{he}T_{he}) = \frac{c_v}{R}(\dot{p}_h V_h), \tag{16}$$

$$\text{Expansion}: -\dot{Q}_{\mathrm{app}} - \dot{Q}_{\mathrm{leak},d} + c_p\dot{m}_{he}T_{he} = \frac{c_v}{R}(\dot{p}_e V_e) + \frac{c_p}{R}(p_e \dot{V}_e) - \dot{W}_{\mathrm{gsh},d} - \dot{W}_{\mathrm{sf},d}, \tag{17}$$

The parasitic losses are applied to the energy equation as follows: the compression and expansion spaces are in an adiabatic condition, meaning that no heat energy is allowed in or out. In the compression space, the enthalpy loss of the working gas occurs through seal clearance between the DP and PP, while in the expansion space, enthalpy loss occurs through DP seal clearance into the compression space. Note that the DP rod has a very small cross-section compared to DP and PP [35] such that the seal leakage loss of the DP rod can be ignored. The gas spring hysteresis loss occurring

in the PP bounce space is included in the loss in the compression space. Also, the appendix gap loss for the DP and the spring hysteresis loss in the DP bounce space are included in the loss in the expansion space.

The cooler, regenerator, and heater spaces do not change in terms of the volume, so no work occurs. Flow friction losses due to forced convection occur in the cooler, regenerator, and heater. In the regenerator, reheat loss occurs due to the limited heat transfer during the cooling and heating processes under the reciprocating flow of the working gas.

The pressure in each space is defined with Eqs. (18)–(22), where the pressure in the compression space is assumed as the baseline pressure, and the pressures in the cooler, regenerator, heater, and expansion space are defined using the pressure drop. As shown in Figure 1, the pressure in each space is the average value of the pressure distribution in each space considering the pressure drop [13].

$$p_c = p, \tag{18}$$

$$p_k = p_c + \frac{\Delta p_k}{2}, \tag{19}$$

$$p_{r1} = p_k + \frac{(\Delta p_k + \Delta p_{r1})}{2}, \tag{20}$$

$$p_{r10} = p_{r9} + \frac{(\Delta p_{r9} + \Delta p_{r10})}{2},$$

$$p_h = p_{r10} + \frac{(\Delta p_{r10} + \Delta p_h)}{2}, \tag{21}$$

$$p_e = p_h + \frac{\Delta p_h}{2}. \tag{22}$$

The pressure drops are calculated considering flow frictions and geometries of the heat exchangers and the regenerator [33].

$$\Delta p = \frac{2 Re f_f \mu u V}{A_{fr} d_h^2}. \tag{23}$$

Note that the pressure in each space is different due to the pressure drop, while the rate of pressure change in each space does not have a large difference in actual Stirling engines [13]. Therefore, it is assumed that $\dot{p} \approx \dot{p}_c \approx \dot{p}_k \approx \dot{p}_r \approx \dot{p}_h \approx \dot{p}_e$. Based on this assumption, the equation used to determine the rate of pressure change for the working spaces overall is obtained by adding all of the energy equations of Eqs. (13)–(17), such that

$$\dot{p} = \frac{\left[R\left(\sum \dot{Q}_i - \sum \dot{Q}_{reh,n} - \sum \dot{Q}_{hf,i} - \dot{Q}_{app} + \sum \dot{W}_{gsh,j} + \sum \dot{W}_{sf,j} \right) - c_p \left(p \dot{V}_c + p \dot{V}_e \right) \right]}{c_v \sum V_z}, \tag{24}$$

where $i = k, r1 \cdots r10, h$, n= $r1 \cdots r10$, $j = d, p$, and $z = c, k$, $r1 \cdots r10, h, e$.

On the other hand, the mass flow rate of the working gas passing through the boundary of each space is defined as

Eqs. (25)–(28) by arranging the energy Eqs. (13)–(16) for the mass flow rate terms.

$$-\dot{m}_c = \dot{m}_{ck} = -\frac{1}{RT_{ck}} \left(\frac{\dot{p}_c V_c}{\gamma} + p_c \dot{V}_c \right) + \frac{\left(\dot{Q}_{leak,d} + \dot{Q}_{leak,p} + \dot{W}_{gsh,p} + \dot{W}_{sf,p} \right)}{c_p T_{ck}}, \tag{25}$$

$$\dot{m}_{kr1} = \frac{\left\{ \dot{Q}_k - \dot{Q}_{hf,k} + c_p \dot{m}_{ck} T_{ck} - c_v/R(\dot{p}_k V_k) \right\}}{c_p T_{kr1}}, \tag{26}$$

$$\dot{m}_{r1,r2} = \frac{\left\{ \dot{Q}_{r1} - \dot{Q}_{reh1} - \dot{Q}_{hf,r1} + c_p \dot{m}_{kr1} T_{kr1} - c_v/R(\dot{p}_{r1} V_{r1}) \right\}}{c_p T_{r1,r2}},$$

$$\vdots$$

$$\dot{m}_{r10h} = \frac{\left[\dot{Q}_{r10} - \dot{Q}_{reh,10} - \dot{Q}_{hf,r10} + c_p \dot{m}_{r9r10} T_{r9r10} - c_v/R(\dot{p}_{r10} V_{r10}) \right]}{c_p T_{r10h}}, \tag{27}$$

$$\dot{m}_e = \dot{m}_{he} = \frac{\left\{ \dot{Q}_h - \dot{Q}_{hf,h} + c_p \dot{m}_{r10,h} T_{r10,h} - c_v/R(\dot{p}_h V_h) \right\}}{c_p T_{he}}. \tag{28}$$

The mass of the working gas in the space between the heat exchanger and the regenerator is calculated according to the difference in the mass flow rate passing through the interface, as shown in Eqs. (29)–(31).

$$\dot{m}_k = \dot{m}_{ck} - \dot{m}_{kr1}, \tag{29}$$

$$\dot{m}_{r1} = \dot{m}_{kr1} - \dot{m}_{r1r2}, \tag{30}$$

$$\vdots$$

$$\dot{m}_{r10} = \dot{m}_{r9r10} - \dot{m}_{r10h},$$

$$\dot{m}_h = \dot{m}_{r10h} - \dot{m}_{r10he}. \tag{31}$$

2.3.4. Power and Efficiency Calculation. All state quantities of the volume, temperature, pressure, and mass of the working gas in each space yield the engine power output and efficiency as well as the heat supply and removal of the engine. The heat flow of the cooler, regenerator, and heater that is exchanged with the working gas by forced convection is calculated using the convective heat transfer equations below.

$$\dot{Q}_k = h_k A_{wt,k} (T_{wk} - T_k), \tag{32}$$

$$\dot{Q}_{r1} = h_{r1} A_{wt,r1} (T_{wr1} - T_{r1}),$$

$$\vdots \tag{33}$$

$$\dot{Q}_{r10} = h_{r10} A_{wt,r10} (T_{wr10} - T_{r10}),$$

$$\dot{Q}_h = h_h A_{wt,h} (T_{wh} - T_h). \tag{34}$$

In these equations, h is the heat transfer coefficient in each space of the heat exchanger part.

TABLE 2: Correlation equations of the tube-type heat exchanger.

Parameter	Model	Correlation
Friction factor	Rogers and Mayhew [36, 37]	$\text{Re} \leq 2000, f_f = 16\,\text{Re}^{-1}$ $2000 < \text{Re} \leq 4000, f_f = 7.343 \times 10^{-4}\,\text{Re}^{0.3142}$ $\text{Re} > 4000, f_f = 0.0791\,\text{Re}^{-0.25}$
Heat transfer coefficient	Reynolds simple analogy [38] (Re ≤ 4000)	$h = \left\lvert \dfrac{f_f g c_p}{2\text{Pr}} \right\rvert$
	Chilton-Colburn J-factor analogy [39] (Re > 4000)	$h = \left\lvert \dfrac{f_f g c_p}{2\text{Pr}^{2/3}} \right\rvert$

TABLE 3: Correlation equations of the regenerator.

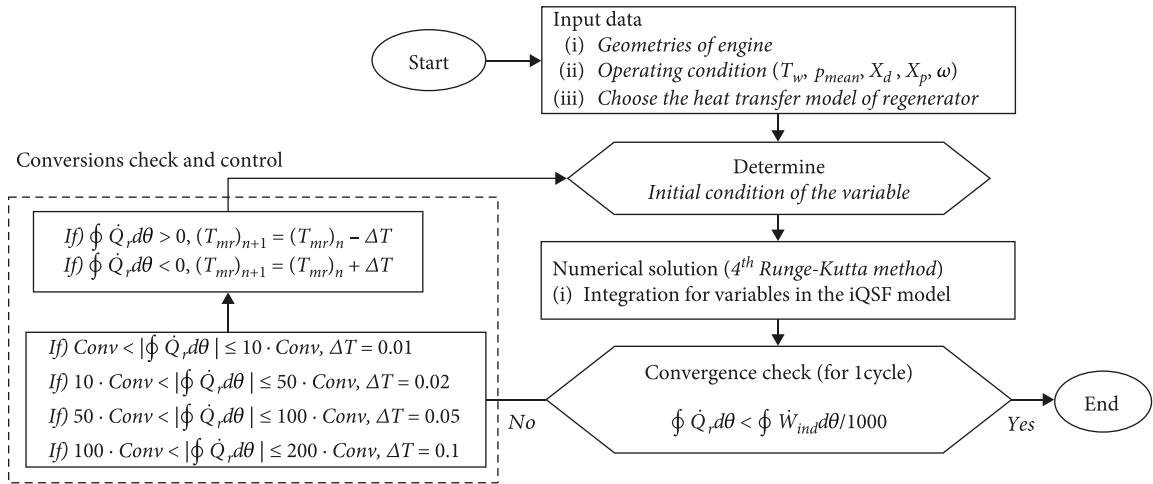|	Kays and London [40]	Tanaka et al. [41]
Flow type	Steady flow	Oscillating flow
Regenerator type	Woven wire (stainless steel)	Woven wire (stainless steel)
Wire diameter	0.27 mm	0.05-0.23 mm
Porosity	0.602-0.832	0.645-0.754
Friction factor	$f_f = 54\,\text{Re}^{-1} + 1.43\,\text{Re}^{-0.52}$	$f_f = \dfrac{\left(175\,\text{Re}^{-1} + 1.6\right)}{4}$
Heat transfer coefficient	$h_r = 0.46\,\text{Re}^{0.6}\left(k_{\text{gas}}/d_h\right)$	$h_r = 0.33\,\text{Re}^{0.67}\left(k_{\text{gas}}/d_h\right)$

FIGURE 2: Flow chart of the iQSFM calculation procedure.

The indicated power is defined as the sum of the outputs of the expansion space and compression space, and the mechanical power output is calculated as the value obtained by subtracting the gas spring hysteresis loss and the seal friction loss, which are output losses, from the indicated power.

$$\dot{W}_{\text{ind}} = p\dot{V}_c + p\dot{V}_e, \tag{35}$$

$$\dot{W}_{\text{mech}} = \dot{W}_{\text{ind}} - \left(\dot{W}_{\text{gsh},j} + \dot{W}_{\text{sf},j}\right). \tag{36}$$

where $j = $ dp, pp.

The indicated efficiency and mechanical efficiency are calculated using the following equations, where the heat conduction loss through the engine head cylinder is considered.

$$\eta_{\text{ind}} = \frac{\dot{W}_{\text{ind}}}{\dot{Q}_h + \dot{Q}_{\text{cond}}}, \tag{37}$$

$$\eta_{\text{mech}} = \frac{\dot{W}_{\text{mech}}}{\dot{Q}_h + \dot{Q}_{\text{cond}}}. \tag{38}$$

2.4. Friction Factor and Heat Transfer Models. In order to solve the iQSFM established above, the friction coefficient of
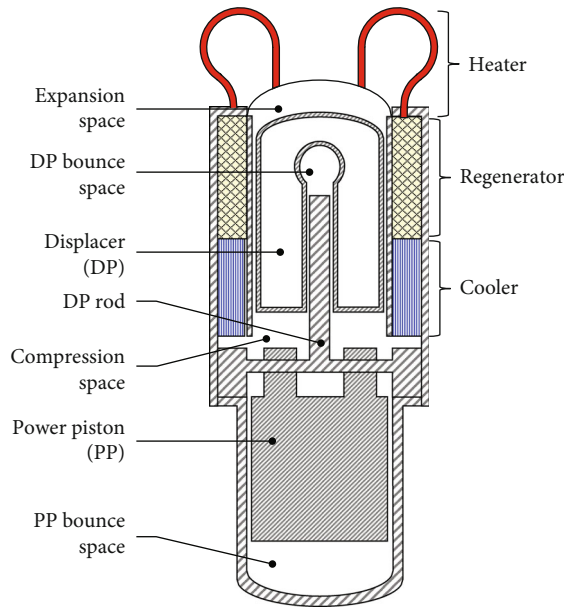
FIGURE 3: Schematic of the RE-1000 engine (built by NASA).

the heat exchanger and regenerator and the heat transfer coefficient between the wall and the working gas must be determined and reflected in the heat input/removal heat and pressure drop calculations.

The friction coefficient and heat transfer coefficient vary depending on the heat exchanger shape, flow type, and temperature conditions.

The fanning friction factor for the tube-type heat exchanger covered in this paper is calculated from the friction coefficient correlation equation with respect to the Reynolds number, which is based on Moody's chart, ignoring the surface roughness [36, 37]. In addition, the heat transfer coefficient in the internal pipe flow was defined using the Reynolds simple analogy and J-factor analogy according to the Reynolds number [38, 39]. The Reynolds simple analogy is a theoretical equation that uses the similarity between the forced convection heat transfer and friction coefficient and defines the heat transfer coefficient using the friction coefficient derived through an empirical equation. The Reynolds simple analogy shows high accuracy under laminar flow conditions. Similarly, the J-factor analogy is a theoretical equation that uses the correlation between the forced convection heat transfer and fluid friction coefficient and shows high accuracy under turbulent flow conditions. Table 2 summarizes the correlation models for the friction factor and heat transfer coefficient for the tube-type heat exchanger. Here, g is the mass flux of the working gas.

The fanning friction factor and convective heat transfer coefficient of the regenerator are calculated with reference to studies that measured them experimentally according to the flow rate, temperature, and pressure drop of the flow inside the regenerator [40, 41]. In the reference paper, the fanning friction factor was calculated through a pressure drop measurement, and the heat transfer coefficient was defined through a dimensional analysis using the relation-

ship between the Nusselt number and the Reynolds number derived from the experiment. Table 3 shows the friction coefficient and heat transfer coefficient of the regenerator for a steady flow and an oscillating flow, where k_{gas} and d_h are the heat conductivity and hydraulic diameter, respectively.

2.5. Model Solution Algorithm. Figure 2 presents a flow chart of the solution procedure of iQSFM. First, the engine geometry data (i.e., heat exchanger/regenerator geometry and piston cross-sectional area) and the operating conditions of the heat exchanger wall temperature (heat supply condition), engine average pressure (working gas charging condition), piston amplitude/frequency (piston motion condition), and the regenerator model (steady flow or oscillating flow) are entered. For reference, the iQSF model does not consider changes in average pressure due to gas temperature changes, and the average pressure is kept constant as an input value.

Subsequently, the initial value of the iQSFM variable is determined, and the ordinary differential equation of iQSFM is numerically integrated for each time step using the fourth-order Runge-Kutta method. The time step size of iQSFM is 1 cycle/100, and convergence is checked once per cycle.

The convergence criterion for this numerical analysis is that the net heat transfer of the regenerator matrix during one cycle reaches within 0.1% of the indicated power. Here, the net heat transfer of zero means that the Stirling cycle has reached a periodic steady state. If the numerical analysis does not converge, the regenerator matrix temperature is reset according to the net heat transfer amount of the regenerator, and the calculation is repeated. In detail, when the net heat transfer is greater than zero, the temperature of the regenerator matrix is reduced. This reduces the heat transfer from the regenerator matrix to the working gas, approaching a net heat transfer of zero. Conversely, when the net heat transfer is less than zero, the temperature of the regenerator matrix is increased.

3. Model Validation

3.1. RE-1000 Engine for Model Validation. The proposed iQSFM is verified using the experimental data of the RE-1000, free-piston Stirling engine developed by NASA [42]. As shown in Figure 3, it is a beta-type FPSE in which the DP and PP are located on the same axis with the heat exchange part composed of a tube-type heater, a fin-type cooler, and a woven mesh-type regenerator. Also, the DP and PP bounce spaces act as gas springs for each piston. The mechanical output power is measured using a dashpot load.

For model verification, the operating conditions and experimental results of #1011 given in the literature [42], which were the reference RE-1000 test cases in other studies, were used. The detailed design parameters for the RE-1000 as used in iQSFM are presented in Table 4.

3.2. Model Validation Using RE-1000. Figure 4 shows the calculated mean heat flow rate of the regenerator over the iterations of iQSFM. The red dotted line is the mean heat flow rate of all ten regenerator cells, while the other dotted lines are the mean heat flow rates of the odd-numbered

TABLE 4: Design parameters and operating conditions of the RE-1000 engine for the #1011 test [42].

Design parameter		Value	Unit
Heater (tube type)	Number of tubes	34	
	Tube inner diameter	2.36	mm
	Heater volume	27.33	cm^3
Cooler (fin type)	Fin number	135	
	Cooler volume	20.43	cm^3
Regenerator (woven mesh type)	Porosity	75.9	%
	Wire diameter	0.0889	mm
	Void volume	56.37	cm^3
Volume	Expansion space	27.74	cm^3
	Compression space	54.8	cm^3
	DP bounce space	30.79	cm^3
	PP bounce space	2615	cm^3
Displacer	Diameter	56.4	mm
	Appendix gap clearance	0.381	mm
	Seal clearance	0.033	mm
DP	Diameter	56.4	mm
	Appendix gap clearance	0.381	mm
	Seal clearance	0.033	mm
DP rod	Diameter	16.7	mm
	Seal clearance	0.03	mm
PP	Diameter	57.2	mm
	Seal clearance	0.033	mm
Operating condition	Heater temperature	600	˚C
	Cooler temperature	25	˚C
	Charge pressure	70.6	bar
	Frequency	30	Hz
	DP stroke	24.5	mm
	PP stroke	28	mm
	DP-PP phase angle	57.5	˚

regenerator cells. The flow model assumes an oscillating flow. As a result, the net heat transfer of the regenerator over one cycle converged to less than 0.1% (-0.82 W) of the indicated power (1286.8 W) when 84 cycles were repeatedly calculated.

Figure 5 shows the predicted thermal performance of the RE-1000, showing (a) the heat flow rates of the heater, cooler, and regenerator over the piston crank angle and (b) pressure-volume (PV) diagrams of the expansion and compression spaces.

As shown in Figure 5(a), thermal energy is continuously input to the working gas with a positive mean heat flow rate of 4614.7 W in the heater, as the temperature of the working gas is lower than the wall temperature. Conversely, in the cooler, the temperature of the working gas is higher than the wall temperature, meaning that the heat flow rate has a negative mean value of -3328.7 W. On the other hand, the regenerator stores and releases the heat flow between the working fluid and the regenerator mesh in one cycle. This creates a periodic waveform

with a total heat flow rate close to zero. In particular, it can be seen that the peak value of the heat flow rate of the regenerator is much larger than that of the heater or cooler. This means that most of the heat exchange inside the Stirling engine takes place in the regenerator, demonstrating the importance of the regenerator with regard to how the engine performs.

Figure 5(b) shows PV diagrams of the expansion and compression spaces. The internal area of the PV diagram refers to the work per cycle, and the expansion space and compression space work values are 111.2 J and -68.3 J, respectively. Multiplied by the operating frequency of 30 Hz, the indicated power is determined to be 1285.7 W by subtracting the compression space power from the expansion space power. The pure heat input to engine (4614.7 W -3328.7 W) is nearly identical to the output power (1285.7 W). Note that the rejected heat from the cooler includes all of the thermal losses inside the engine.

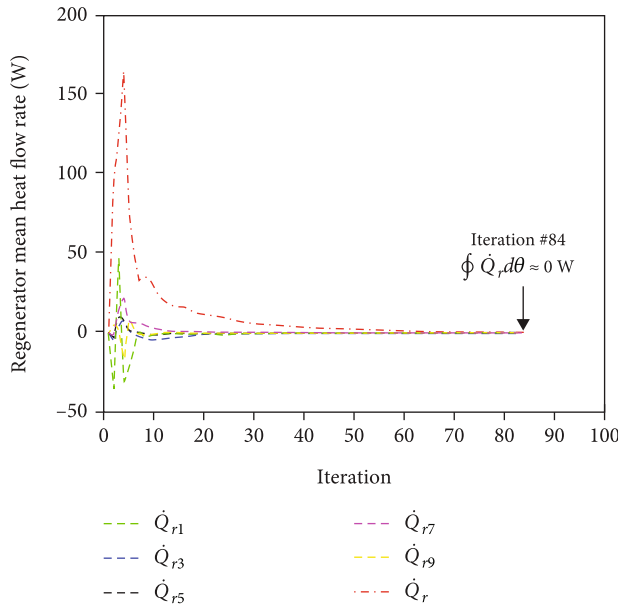Figure 6 presents the energy flow diagram of the RE-1000 as predicted through iQSFM. The heat input of

FIGURE 4: Convergence behavior of the regenerator mean heat flow rate for iQSFM.

4614.7 W has a thermal loss of 801.9 W. The external structural conduction of 28.4 W is directly removed by the cooler through the cylinder wall, not being supplied into the working gas. The reheat loss of the regenerator was 22.8 W, the DP appendix gap loss was 42.7 W, the heat exchanger friction loss was 78.9 W, and, importantly, the seal leakage loss was 657.5 W, which was the largest loss and accounted for 72% of the total loss. The flow friction losses in the heat exchanger consist of 60.5 W in the regenerator, 15.6 W in the heater, and 2.5 W in the cooler. The total amount of heat removed through the cooler, including all of the heat losses, is 3328.7 W.

As a result, the indicated power generated through the Stirling cycle is 1285.7 W. Considering the power loss of 81 W from the seal friction loss and gas spring hysteresis loss, the final mechanical power is 1204.6 W. The gas spring hysteresis loss in the PP bounce space was predicted to be greater than that of the DP bounce space, with values of 73.0 W for PP and 6.84 W for DP.

Table 5 shows a comparison of the analysis results of the Formosa model [43], QSFM [13], and iQSFM with identical experimental conditions for RE-1000 (#1011). The Formosa model is different from the QSFM and iQSFM in that it predicts the piston motion (amplitude, phase, and frequency) by combining the first-generation Schmidt model with the free-piston dynamics model. The QSFM is the original model referenced in Urieli [13], where the loss model is removed from iQSFM here. Both QSFM and iQSFM used the Tanaka model for the oscillating flow in the regenerator.

As a result, iQSFM predicts the experimental results with higher accuracy than QSFM in terms of both the power output and the thermal efficiency. In particular, the power output error of QSFM is large at 66.7%, while that of iQSFM is improved to less than 25%.

On the other hand, the Formosa model shows an error of 6.8%, which predicts the experimental results most accurately among the three models. However, the heat input and rejection predictions are smaller than the experimental results and have larger errors. This appears to be due to the excessive heat exchange performance of the idealized heat exchanger model in the Schmidt model.

Overall, iQSFM shows better prediction accuracy than QSFM in terms of the heat supply and removal, the engine output, and the efficiency. Compared to the Formosa model, iQSFM appears to have a similar level of prediction accuracy and especially higher accuracy when predicting the thermal efficiency.

3.3. Comparison of Correlation Equations of the Regenerator. Figure 7 shows the analysis results of the Fanning friction factor and convective heat transfer coefficient in the regenerator using the Kays and London model for a steady flow and the Tanaka model for an oscillating flow and their comparison to experimental outcomes.

The friction factor of the Tanaka model is predicted to be about 7.8% larger than that of the Kays and London model. According to Muto and Nakane's study of an oscillating flow in a pipe [45], an oscillating flow has a larger velocity gradient at the wall and center of the pipe than a steady flow, and the larger velocity gradient generates high shear stress and increases the pressure drop. Conversely, the heat transfer coefficient of the Tanaka model is approximately 5.6% smaller than that of the Kays and London model because the oscillating flow has a smaller Reynolds number due to its slower average flow rate compared to that of a steady flow.

Table 6 shows a comparison of the engine performance according to the regenerator correlation equations for the Kays and London model and the Tanaka model. According to the maximum heat transfer coefficient and friction coefficient above, the Kays and London model predicts greater heat exchange performance and a smaller amount of friction loss in the regenerator. As a result, the heat input and rejection predicted with the Kays and London model were slightly smaller than those predicted with the Tanaka model because less heat transfer was required due to the higher performance of the regenerator. In addition, the power output predicted with the Kays and London model was slightly larger due to the smaller loss in the regenerator.

As a result, compared to the experimental results, the Tanaka model predicts the power output and thermal efficiency more accurately than the Kays and London model because the Kays and London model overestimates the engine performance more with smaller heat input and larger power output values.

4. Parameter Study of RE-1000 Using iQSFM

In this chapter, a parameter study of RE-1000 using iQSFM was conducted to examine the engine performance and loss characteristics regarding the key design factors, in this case, the heater, regenerator, and seal clearance. Table 7 shows the reference values and ranges of the design factors used in the parameter study. The Tanaka model was applied to the regenerator correlation.
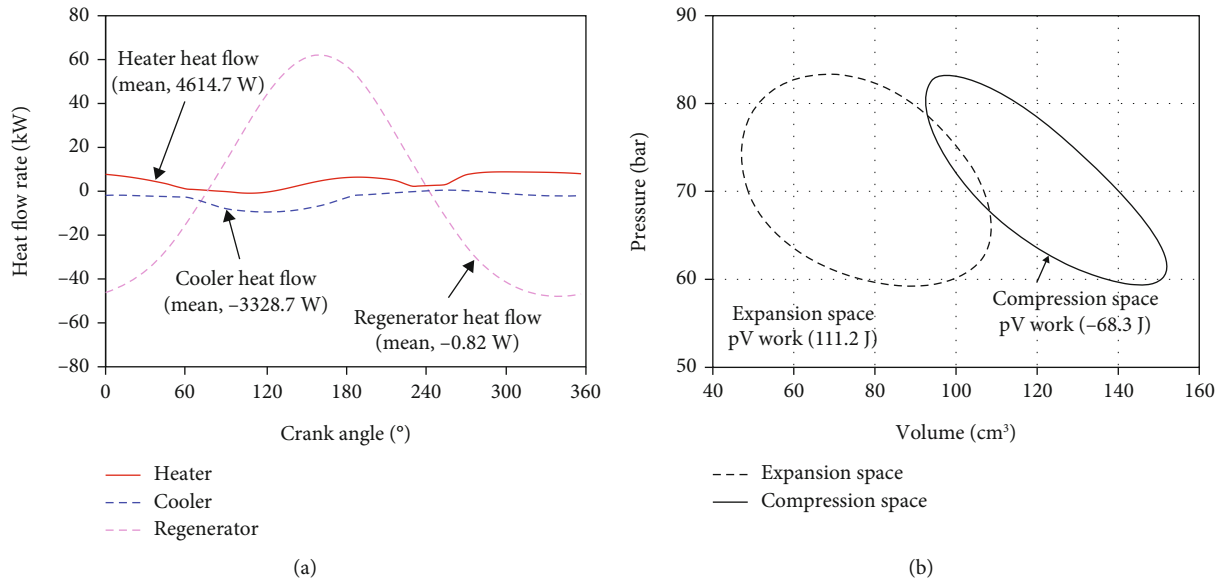
FIGURE 5: Predicted thermal performance of the RE-1000: (a) heat flow rates of the heater, cooler, and regenerator over the piston crank angle and (b) pressure-volume (PV) diagrams of the expansion and compression spaces.
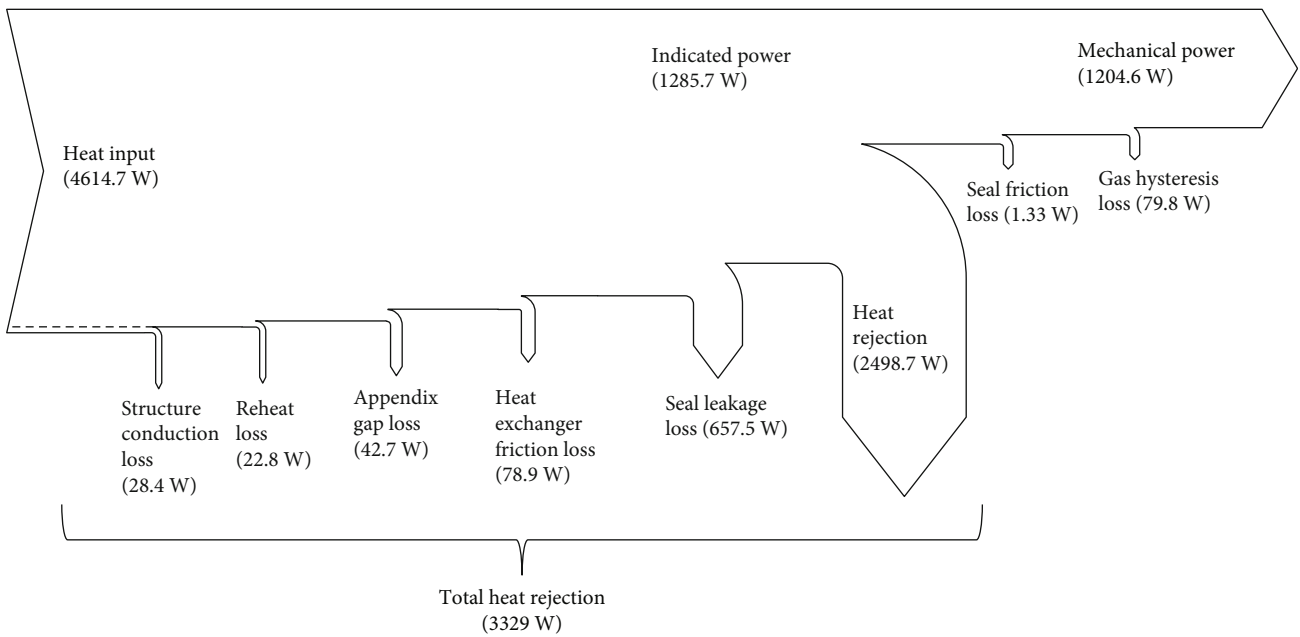

FIGURE 6: Energy flow diagram of RE-1000 as predicted through the iQSFM analysis.

TABLE 5: Comparison of various model results.

	Formosa [43]	QSFM [44]	iQSFM	Experiment (#1011)
Heat in (W)	3777 (-6.5%)	4949 (22.6%)	4614.7 (14.3%)	4038
Heat rejection (W)	2107 (-30.5%)	2742 (-9.6%)	3329 (9.8%)	3032
Indicated power (W)	1100 (6.8%)	1717 (66.7%)	1285.7 (24.8%)	1030
Indicated efficiency (%)	29.2(14.5%)	34.5 (35.3%)	27.7 (8.6%)	25.5

4.1. Heater Parameters. Figure 8 shows the results of the analysis for (a) the pressure drop and heat transfer coefficient, (b) the indicated power output and thermal effi-ciency, (c) total parasitic losses and heat in/rejection, and (d) major parasitic losses as the number of heater tubes increases. Minor losses shown in Figure 8(c) are the sum
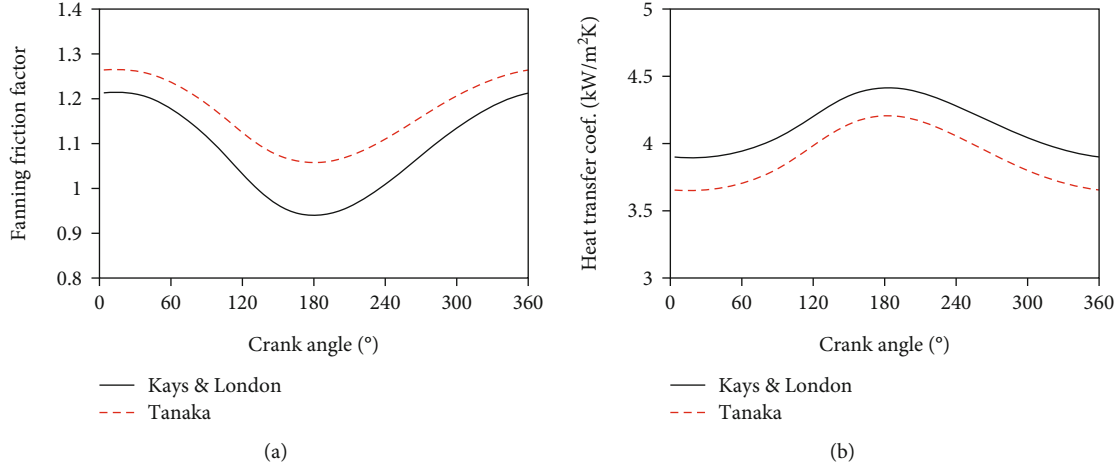
FIGURE 7: Analysis results of (a) the Fanning friction factor and (b) the heat transfer coefficient of the regenerator.

TABLE 6: Comparison of the engine performance for the correlation equation of the regenerator.

	Kays and London model (steady flow)	Tanaka model (oscillating flow)	Experiments (#1011)
Max. heat transfer coef. (kW/m^{2}K)	4.41	4.20	—
Fanning friction factor	1.21	1.27	
Pressure drop (kPa)	49.61 (-17.9%)	51.74 (-14.4%)	60.41
Heat in (W)	4564.3 (13.0%)	4614.7 (14.3%)	4038
Heat rejection (W)	-3148.2 (3.8%)	-3329 (9.8%)	-3032
Indicated power (W)	1301.4 (26.3%)	1285.7 (24.8%)	1030
Efficiency (%)	28.5 (11.8%)	27.7 (8.6%)	25.5

TABLE 7: Parameter study variables for RE-1000.

Parameter	Reference value	Parameter study range	Unit
Number of heater tube	34	6-60	—
Inner diameter of heater tube	2.362	0.962-4.762	mm
Regenerator porosity	0.759	0.689-0.879	—
Regenerator diameter	88.9	68.9-258.9	μm
DP&PP seal clearance	33	3.3-46.2	μm
DP appendix gap	0.381	0.0381-0.762	mm

of head conduction loss, seal friction loss, and gas spring hysteresis loss.

In general, the main design factors of heater tubes are the tube diameter, length, and number. If the diameter and length are fixed and the number of tubes is increased, the cross-sectional area increases and the flow resistance decreases, eventually reducing the pressure drop. On the other hand, the heat transfer coefficient decreases as the flow rate slows down. The analysis results show these characteristics well. As a result, the indicated power and efficiency increase, remain constant, and then decrease slightly as the tube number increases. Parasitic losses change significantly similar to performance when the number of tubes is 20 or less, and the DP leakage loss and HHX flow loss are the key. In other words, a small number of tubes increases the flow resistance of HHX, which increases the DP leakage loss.

Here, total parasitic losses are dominated by the DP and PP leakage loss.

Specifically, the pressure drop is low and relatively constant when there are 20 or more tubes, with the HHX flow friction loss converging to almost 0 W. Also, the indicated power and thermal efficiency also remain high and mainly constant. However, if there are too many tubes, the heat transfer coefficient is reduced more, resulting in poor performance of the heat exchanger and a relatively slight decrease in the engine power and efficiency.

As a result, there are 34 heater tubes for RE-1000 here, which can be seen as an optimized design from a performance point of view.

Figure 9 shows the results of the analysis of (a) the pressure drop and heat transfer coefficient, (b) the indicated power output and thermal efficiency, (c) total parasitic losses
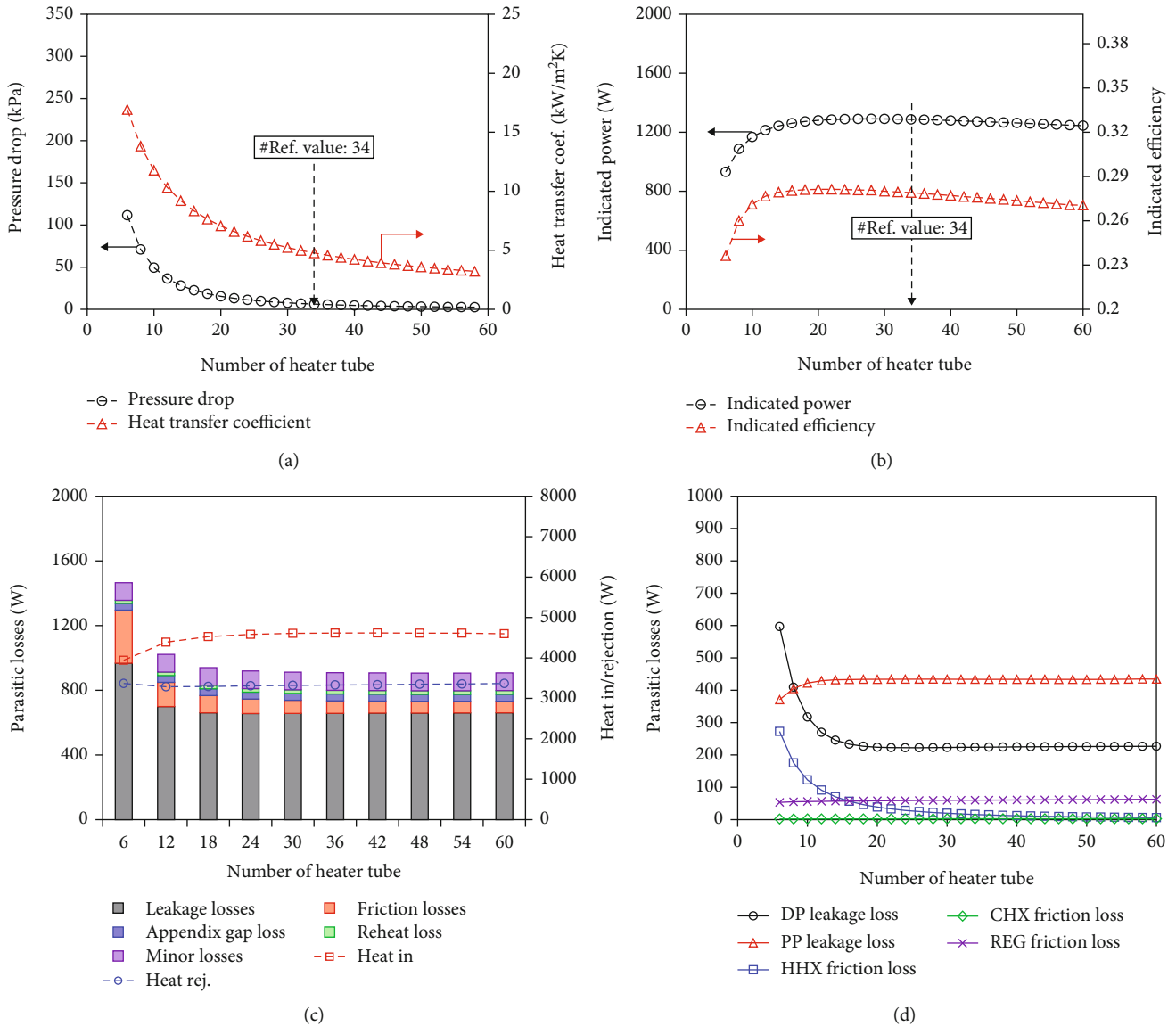
FIGURE 8: Predicted (a) pressure drop and heat transfer coefficient, (b) indicated power and efficiency, (c) total parasitic losses and heat in/rejection, and (d) major parasitic losses versus the number of heater tubes.

and heat in/rejection, and (d) major parasitic losses as the inner diameter of the heater tube increases.

When the inner diameter increases, the pressure drop and heat transfer coefficient decrease rapidly. Because the inner diameter of the tube changes the flow area of the working gas, the trend is similar to the analysis result in Figure 8. The pressure drop and heat transfer coefficient are more sensitive to the inner diameter than the number of tubes given that an increase in the inner diameter increases the cross-sectional area according to the order of square. Likewise, the parasitic losses also show the similar trends, with the DP leakage loss and the HHX flow friction loss changing more. As a result, the engine output and efficiency increase rapidly and then decrease significantly as the tube diameter increases.

Particularly, the pressure drop converges to zero when the inner diameter of the tube is around 2 mm. Accordingly,

the HHX flow friction loss is minimized in the vicinity of an inner diameter of 2 mm, resulting in maximum output and efficiency. When the inner diameter is greater than 2 mm, the heat transfer coefficient decreases continuously and the performance deteriorates. The inner diameter of the heater tube of RE-1000 is 2.362 mm, which can be seen as an optimal design that satisfies both low-pressure drop and high heat transfer coefficient.

4.2. Regenerator Parameter. The main design factors of the regenerator are the regenerator type, porosity, wire diameter, and wire material. The regenerator matrix material of RE-1000 is 304 stainless steel, and the type is a knitted woven wire mesh.

Figure 10 shows the analysis results of (a) the pressure drop and heat transfer coefficient, (b) the indicated power and efficiency, (c) total parasitic losses and heat input/
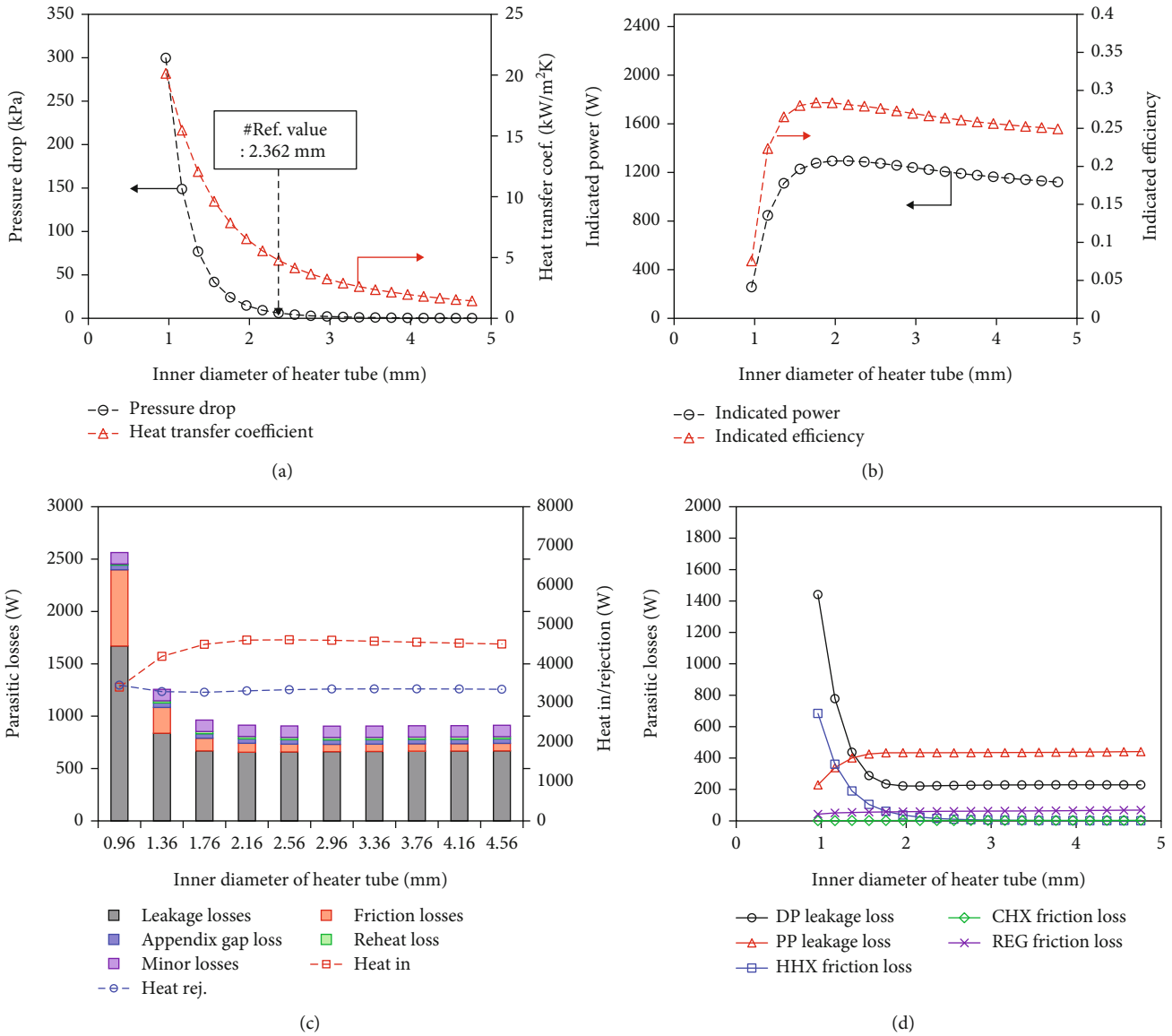
FIGURE 9: Predicted (a) pressure drop and heat transfer coefficient, (b) indicated power and efficiency, (c) total parasitic losses and heat in/rejection, and (d) major parasitic losses versus the inner diameter of the heater tube.

rejection, and (d) major parasitic losses as the regenerator porosity increases.

In general, as the porosity of the regenerator increases, the gas flow area increases, so that the pressure drop decreases. However, the heat capacity also decreases due to reductions in the regenerator material, which reduces the heat transfer coefficient. In other words, as the porosity changes, the pressure drop and the heat capacity have a trade-off relationship regarding engine performance.

As a result, the total parasitic losses decrease as the porosity increases because the DP seal leakage loss is decreased significantly due to the reduced flow resistance of the regenerator.

The reheat loss decreases as the heat capacity increases because the heat is stored for a limited time during approximately half of a cycle and must be released during the other half of the time. Therefore, as the porosity increases for a given regenerator volume, the heat capacity of the matrix decreases, and the reheat loss also increases [46]. On the other hand, the flow friction loss decreases along with the pressure drop due to the effect of the increase in the total flow channel area as the porosity increases.

In summary, as the porosity increases in the given factor range of 0.69 to 0.88, the increase in the reheat loss is greater than the decrease in the flow friction loss. Therefore, the indicated power and efficiency tend to decrease. In addition, as the porosity increases, the increase in heat rejection becomes greater than the heat input, thus greatly reducing the engine performance. As a result, the maximum efficiency is found at an approximate porosity level of 0.73. The regenerator porosity of RE-1000 is 0.759, which is close to the porosity predicted by iQSFM to generate maximum efficiency.

Figure 11 shows the analysis results of (a) the pressure drop and heat transfer coefficient, (b) the indicated power
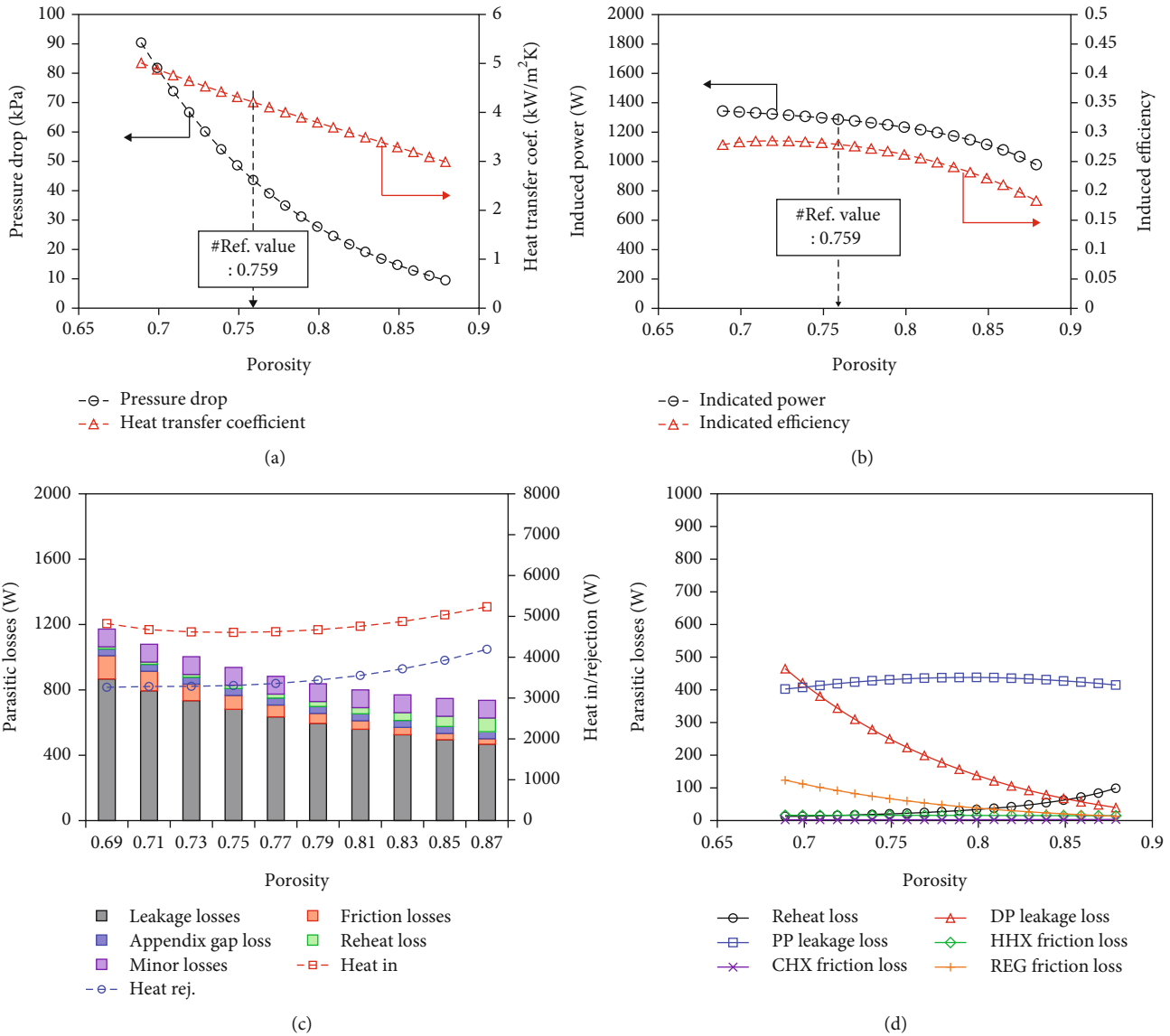
(a)

(b)

(c)

(d)

FIGURE 10: Predicted (a) the pressure drop and heat transfer coefficient, (b) indicated power and efficiency, (c) total parasitic losses and heat in, and (d) major parasitic losses versus the regenerator porosity.

and efficiency, (c) total parasitic losses and heat in/rejection, and (d) major parasitic losses as the regenerator wire diameter increases.

When the wire diameter increases with the porosity maintained, the pressure drop decreases because the total surface area of the wire matrix and the complexity of the gas flow passage decrease, and the heat transfer coefficient decreases as well. As a result, the total parasitic loss decreases due to significant decreases in the DP seal leakage loss, as in the case of porosity.

The reheat loss increases when the wire diameter increases because it is difficult for heat flow to penetrate to the center of the wire diameter in a short time. The flow friction loss increases rapidly as the diameter of the wire decreases, along with the pressure drop.

In the analysis range of this factor from $60\,\mu m$ to $260\,\mu m$, the engine power and efficiency decrease relatively uniformly due to the negative effect of reheat loss. The

regenerator wire diameter of RE-1000 is $88.9\,\mu m$, indicating that it is designed for a higher performance range.

4.3. Piston Seal Parameter. The piston seal has a significant impact on engine performance along with the heat exchangers and regenerator. Theoretically, the smaller the gap, the lower the leakage due to the pressure difference between the two ends of the piston, and the higher the performance. However, if the clearance is too small, the piston and cylinder are difficult to manufacture and align accurately, resulting in mechanical friction and wear in the piston assembly, as well as poor engine operation. On the other hand, gap clearances that are too large lead to severe piston leakage and poor engine performance.

Figure 12 depicts the results of the analysis of (a) the indicated power output, thermal efficiency, and PP seal leakage loss and (b) total parasitic losses and heat input/rejection as the PP seal clearance increases. The seal friction loss due
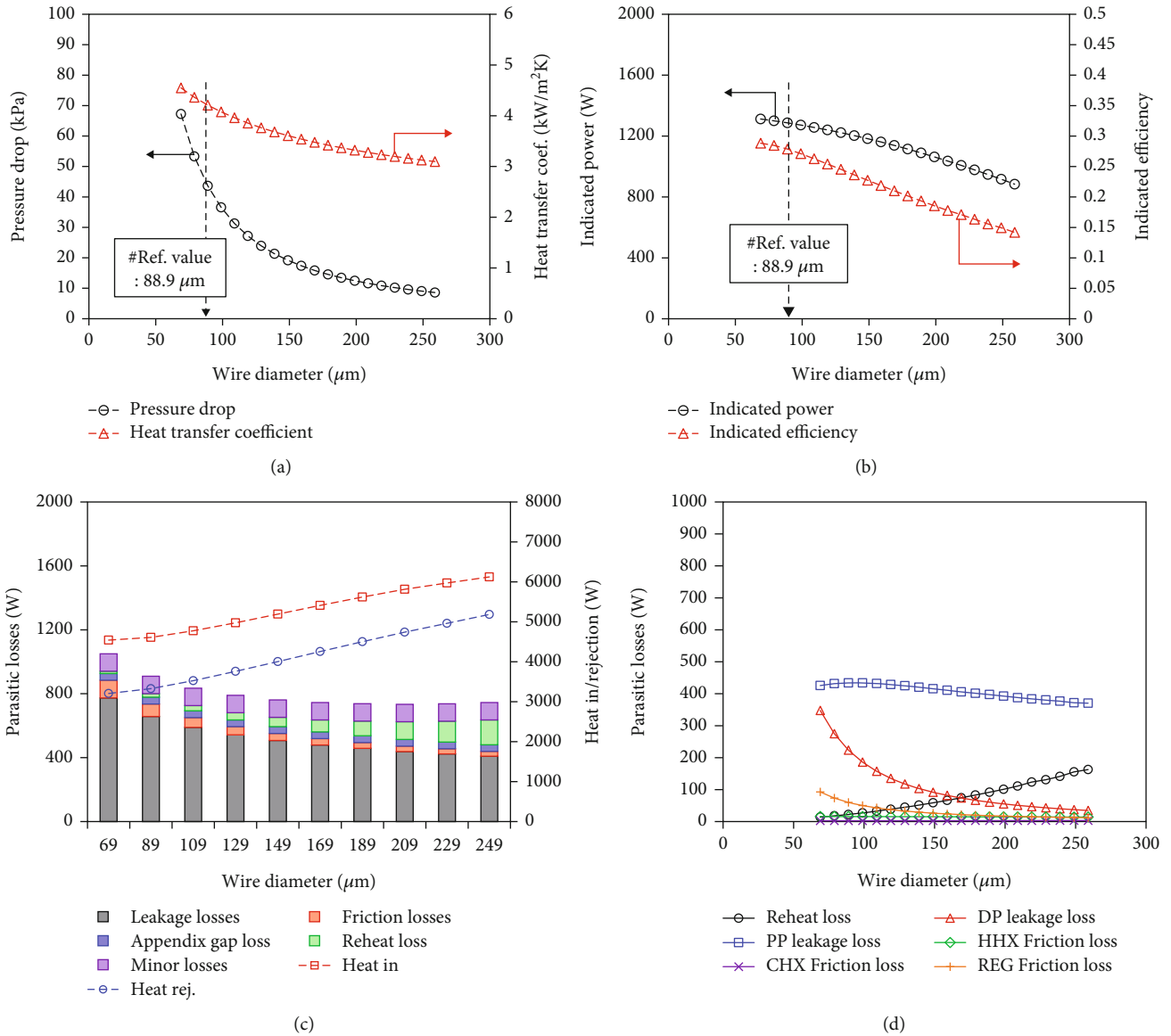
Figure 11: Predicted (a) the pressure drop and heat transfer coefficient, (b) the indicated power and efficiency, (c) total parasitic losses and heat in/rejection, and (d) major parasitic losses versus the regenerator wire diameter.

to the viscous fluid friction in the gap is very small compared to the seal leakage loss, and these results are therefore omitted.

The results show that the seal leakage loss increases in proportion to the square of the seal clearance given that the seal leakage loss is proportional to the flow area. The indicated power and efficiency decrease rapidly as the seal leakage loss increases. Additionally, the heat input decreases significantly with the greater PP seal clearances. The other parasitic losses except for the PP leakage loss remain almost constant.

Figure 13 shows the results of the analysis of (a) the indicated power output, thermal efficiency, and DP seal leakage loss and (b) total parasitic losses and heat input/rejection as the DP seal clearance increases.

As the DP seal clearance increases, the DP seal leakage loss also increases like the PP. However, unlike the PP case,

the indicated power remains almost constant, and the thermal efficiency decreases to some extent.

In addition, when the seal clearances of DP and PP are identical, the leakage loss of DP is analyzed and found to be greater than that of PP. This occurs because a larger enthalpy loss occurs through the DP seal clearance due to a larger temperature difference between both end spaces of the DP.

The leakage loss can be reduced with smaller seal clearances, but in practice, they are manufactured to $50\,\mu$m or less due to manufacturing technology and cost limitations [47]. RE-1000 has the same seal clearances of $33\,\mu$m for DP and PP.

Figure 14 depicts (a) total parasitic losses and heat in/ rejection and (b) the shuttle loss and wall conduction loss for DP as the appendix gap clearance increases. The appendix gap refers to the gap between the piston and cylinder
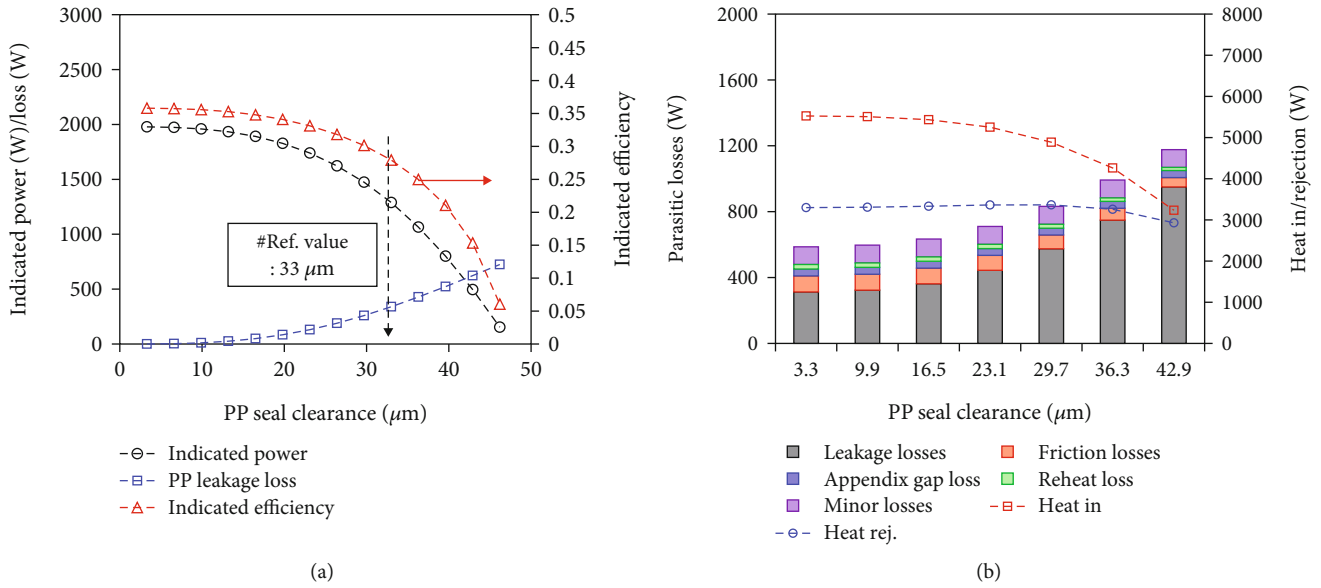
(a)

(b)

FIGURE 12: Predicted (a) indicated power, thermal efficiency, and PP seal leakage loss and (b) total parasitic losses and heat input/rejection versus the PP seal clearance.
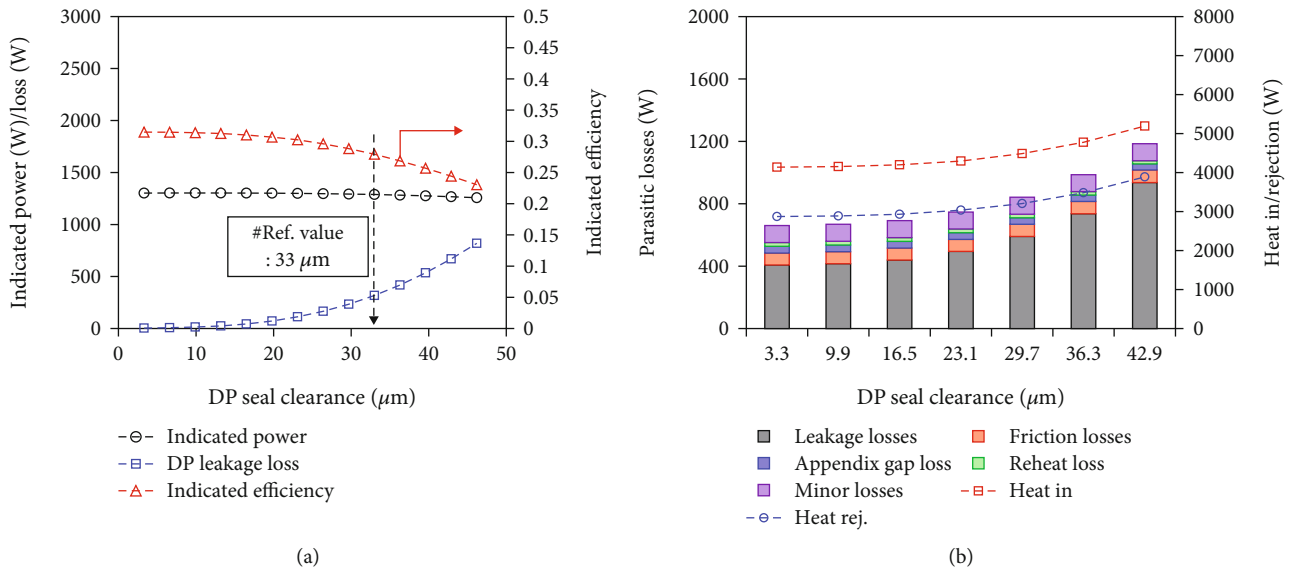

(a)

(b)

FIGURE 13: Predicted (a) indicated power, thermal efficiency, and DP seal leakage loss and (b) total parasitic losses and heat input/rejection versus the DP seal clearance.

liner on the upper part of the DP and is designed to be larger than the seal clearance in the lower part.

When the appendix gap increases, only the appendix gap loss increases, and other losses remain almost unchanged. The appendix gap loss is defined as the sum of the DP wall conduction loss and the shuttle loss. The DP wall conduction loss is affected by the temperature of the expansion and compression spaces and the structural characteristics of the DP. Therefore, it is relatively constant regardless of the appendix gap size and is made to be very small with a thin wall thickness of the DP. On the other hand, the shuttle loss increases rapidly as the appendix gap clearance

decreases because the heat transfer between the piston and cylinder increases. The appendix gap dimension for RE-1000 is 0.381 mm, which is designed to be ten times the seal gap clearance to ensure a low shuttle loss.

Figure 14(c) presents the indicated power and efficiency as the appendix gap clearance increases. When the appendix gap changes, the indicated power remains nearly constant, but the efficiency is affected. This arises because the shuttle loss is heat loss, not flow loss. The heat removed through the shuttle loss is additionally input through the heater to keep the power output constant, but the efficiency decreases due to the increased heat input.
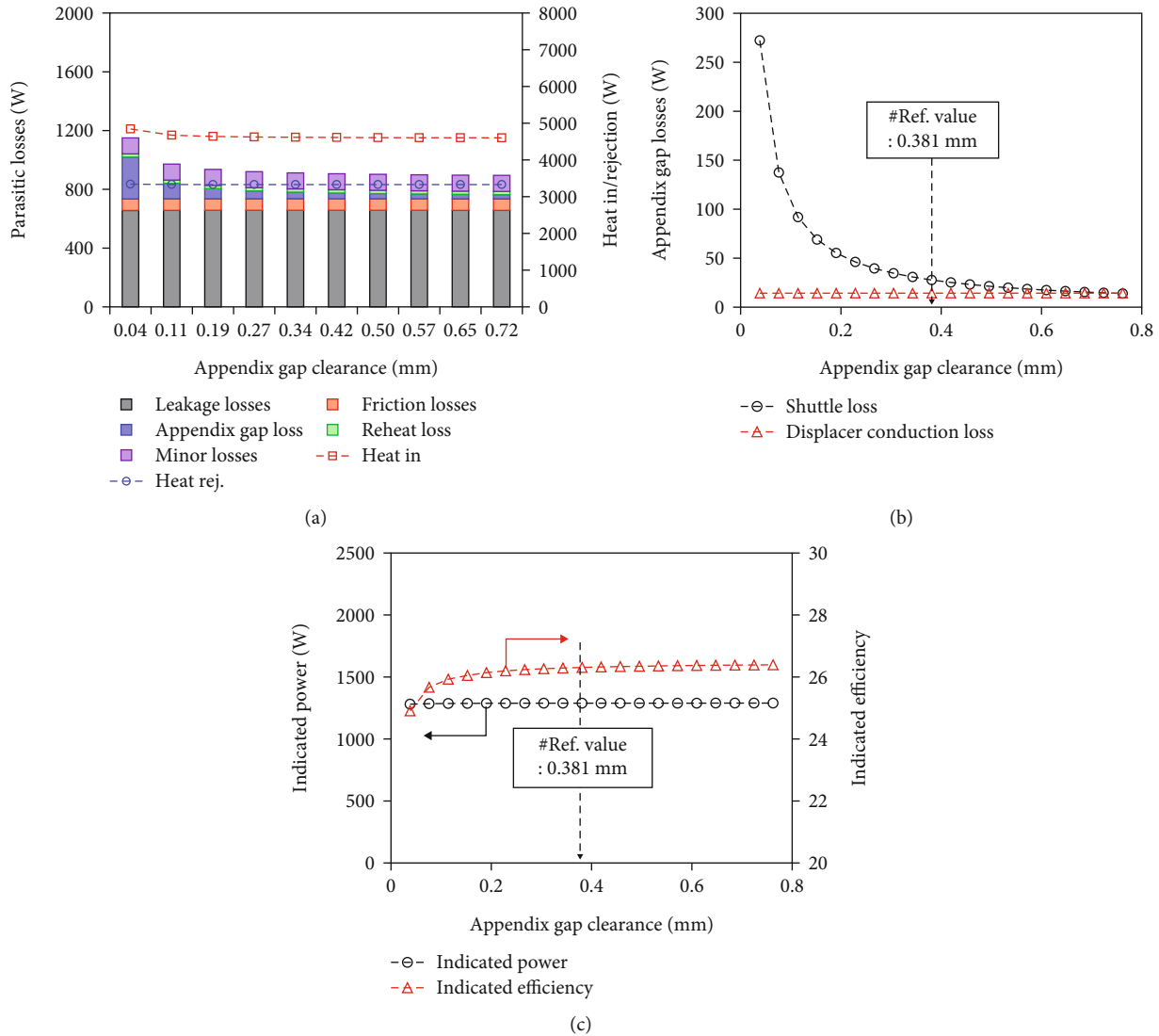
(a)

(b)

(c)

FIGURE 14: Predicted (a) total parasitic losses and heat in, (b) appendix gap losses, and (c) indicated power and efficiency versus the appendix gap clearance.

5. Conclusions

This paper presents the development and validation of iQSFM considering various parasitic losses based on the second-generation QSFM. In addition, iQSFM applied the oscillating flow correlation equation, referring to the actual flow types generated in the regenerator, and these outcomes were compared with an existing steady flow correlation equation. Finally, the engine performance and parasitic losses were analyzed through parameter study of RE-1000 using iQSFM. Through this, the following conclusions were obtained:

(1) The validation of iQSFM was done based on the experimental results of RE-1000, with these outcomes then compared to the predicted results of QSFM. Compared to QSFM, iQSFM significantly improved the prediction accuracy by reducing the engine power error rate from 66.7% to 24.9% and the efficiency error rate from 35.3% to 9.4%. In partic-

ular, the most important parasitic loss with regard to reducing the error rate was the seal leakage loss, which accounted for 72% of the total loss, and it was confirmed that it greatly affects the engine performance

(2) The correlation between a steady flow and an oscillating flow of the regenerator was applied to iQSFM, and these results were compared. When an oscillating flow was applied, the experimental results of the indicated power and efficiency were predicted more accurately than in the steady flow case. However, as a result, major differences in the prediction accuracy of iQSFM depending on the correlation equation of the regenerator cannot be found

(3) It was confirmed through a parameter study using iQSFM that RE-1000 was designed to maximize the engine performance by minimizing losses. At the same time, considering that RE-1000 is an engine

optimally designed by NASA, iQSFM, which predicted the maximum performance near the reference design parameters of RE-1000, has secured value as a tool for designing and optimizing a Stirling engine

Nomenclature

Symbols

A: Area (m^2)
A_{wt}: Wetted area (m^2)
c_{mr}: Regenerator heat capacity (J/K)
c_p: Specific heat at constant pressure (J/kg·K)
c_v: Specific heat at constant volume (J/kg·K)
d: Diameter (m)
d_h: Hydraulic diameter (m)
f_f: Fanning friction factor
g: Mass flux (kg/m^2·s)
H: Gas enthalpy (J)
h: Convective heat transfer coefficient (W/m^2·K)
h_{app}: Appendix gap clearance (mm)
h_{sl}: Seal clearance (mm)
k: Thermal conductivity (W/m·K)
L: Length (m)
m: Mass (kg)
$\dot{m}_{in}$: Inlet mass flow rate of working gas (kg/s)
$\dot{m}_{out}$: Outlet mass flow rate of working gas (kg/s)
Pr: Prantl number
p: Pressure (Pa)
Δp: Pressure drop (Pa)
Q: Heat (J)
$\dot{Q}$: Incoming heat into working space or cell (W)
$\dot{Q}_{app}$: Appendix gap loss in DP (W)
$\dot{Q}_{hf}$: Flow friction loss in heat exchanger (W)
$\dot{Q}_{leak}$: Leakage loss in PP or DP (W)
R: Gas constant (J/kg·K)
Re: Reynolds number
T: Temperature (K)
T_{in}: Inlet temperature of working gas (K)
T_{out}: Outlet temperature of working gas (K)
T_w: Wall temperature (K)
t: Time (s)
u: Gas velocity (m/s)
V: Volume (m^3)
v: Piston velocity (m/s)
W: Work (J)
$\dot{W}$: Rate of work done by working gas (W)
$\dot{W}_{gsh}$: Power loss due to gas spring hysteresis for DP or PP (W)
$\dot{W}_{sf}$: Power loss due to seal friction for DP or PP (W)
X: Amplitude (m).

Greek Letters

α: Phase difference between DP and PP (°)
γ: Specific heat ratio
ε: Effectiveness

η: Efficiency
μ: Viscosity (Pa·s)
ρ: Density (kg/m^3)
ω: Frequency (rad/s).

Subscripts

app: Appendix gap
bd: DP bounce space
bp: PP bounce space
c: Compression space
ck: Compression space to cooler space
cond: Conduction
cyl: Cylinder
d: Displacer
e: Expansion space
fr: Free flow
gas: Working gas
gap: Gap
gsh: Gas spring hysteresis
h: Heater
he: Heater space to expansion space
hf: Heat exchanger flow friction
ind: Indicated
k: Cooler
kr: Cooler space to regenerator space
leak: Leakage
mech: Meachanical
mr: Regenerator matrix
p: Power piston
r: Regenerator
reh: Reheat
rh: Regenerator space to heater space
rod: DP rod
sl: Seal
sf: Seal friction
wk: Cooler wall
wh: Heater wall.

Data Availability

The data used to support the findings of this study are available from the corresponding author upon request.

Conflicts of Interest

The authors declare no conflicts of interest.

Acknowledgments

References

[1] J. Jackson, "Ensuring emergency power for critical municipal services with natural gas-fired combined heat and power (CHP) systems: a cost–benefit analysis of a preemptive strategy," *Energy Policy*, vol. 35, no. 11, pp. 5931–5937, 2007.

[2] B. Thomas, "Benchmark testing of micro-CHP units," *Applied Thermal Engineering*, vol. 28, no. 16, pp. 2049–2054, 2008.

[3] J. Boucher, F. Lanzetta, and P. Nika, "Optimization of a dual free piston Stirling engine," *Applied Thermal Engineering*, vol. 27, no. 4, pp. 802–811, 2007.

[4] I. González-Pino, A. Campos-Celador, E. Pérez-Iribarren, J. Terés-Zubiaga, and J. M. Sala, "Parametric study of the operational and economic feasibility of Stirling micro-cogeneration devices in Spain," *Applied Thermal Engineering*, vol. 71, no. 2, pp. 821–829, 2014.

[5] M. D. d'Accadia, M. Sasso, S. Sibilio, and L. Vanoli, "Micro-combined heat and power in residential and light commercial applications," *Applied Thermal Engineering*, vol. 23, no. 10, pp. 1247–1259, 2003.

[6] D. G. Thombare and S. K. Verma, "Technological development in the Stirling cycle engines," *Renewable and Sustainable Energy Reviews*, vol. 12, no. 1, pp. 1–38, 2008.

[7] V. Kuhn, J. Klemeš, and I. Bulatov, "MicroCHP: overview of selected technologies, products and field test results," *Applied Thermal Engineering*, vol. 28, no. 16, pp. 2039–2048, 2008.

[8] T. Li, D. Tang, Z. Li, J. Du, T. Zhou, and Y. Jia, "Development and test of a Stirling engine driven by waste gases for the micro-CHP system," *Applied Thermal Engineering*, vol. 33-34, pp. 119–123, 2012.

[9] W. T. Beale, *Free Piston Stirling Engines-some Model Tests and Simulations*, SAE Technical Paper, 1969.

[10] R. Dyson, S. Wilson, and R. Tew, "Review of computational Stirling analysis methods," in *2nd International Energy Conversion Engineering Conference*, p. 5582, Providence, Rhode Island, August 2004.

[11] C. West, "Theoretical basis for the Beale number," in *Proc., Intersoc. Energy Convers. Eng. Conf.;(United States)*, vol. 2, Westware Co, Oliver Springs, Tenn, USA, 1981.

[12] G. Schmidt, "The theory of Lehmann's calorimetric machine," *Zeitschrift Des Vereines Deutscher Ingenieure*, vol. 15, pp. 98–112, 1871.

[13] I. Urieli and D. M. Berchowitz, *Stirling cycle engine analysis*, Taylor & Francis, 1984.

[14] T. Finkelstein, *Generalized Thermodynamic Analysis of Stirling Engines*, SAE Technical Paper, 1960.

[15] G. T. Udeh, S. Michailos, D. Ingham, K. J. Hughes, L. Ma, and M. Pourkashanian, "A new non-ideal second order thermal model with additional loss effects for simulating beta Stirling engines," *Energy Conversion and Management*, vol. 206, article 112493, 2020.

[16] M. Babaelahi and H. Sayyaadi, "Simple-II: a new numerical thermal model for predicting thermal performance of Stirling engines," *Energy*, vol. 69, pp. 873–890, 2014.

[17] Y. Timoumi, I. Tlili, and S. Ben Nasrallah, "Design and performance optimization of GPU-3 Stirling engines," *Energy*, vol. 33, no. 7, pp. 1100–1114, 2008.

[18] H. Hosseinzade and H. Sayyaadi, "CAFS: the combined adiabatic–finite speed thermal model for simulation and optimization of Stirling engines," *Energy Conversion and Management*, vol. 91, pp. 32–53, 2015.

[19] T. Finkelstein, "Computer analysis of Stirling engines," *Advances in Cryogenic Engineering*, vol. 20, no. 20, pp. 269–282, 1975.

[20] I. Urieli, C. J. Rallis, and D. M. Berchowitz, "Computer simulation of Stirling cycle machines," in *12th intersociety energy conversion engineering conference*, vol. 2, pp. 1512–1521, Washington, DC, September 1977.

[21] D. M. Berchowitz and C. J. Rallis, "A computer and experimental simulation of Stirling cycle machines," in *13th Intersociety Energy Conversion Engineering Conference*, vol. 3, pp. 1730–1738, San Diego, California, August 1978.

[22] A. Schock, *Nodal Analysis of Stirling Cycle Devices*, Fairchild Space and Electronics Company, 1978.

[23] D. Gedeon, "Sage-object-oriented software for Stirling machine design," in *Intersociety Energy Conversion Engineering Conference*, p. 4106, Monterey, CA, USA, August 1994.

[24] D. Gedeon, *Sage User's Guide: Stirling, Pulse-Tube and Low-T Cooler Model Classes*, Gedeon Associates, 2014.

[25] G. Xiao, Y. Huang, S. Wang et al., "An approach to combine the second-order and third-order analysis methods for optimization of a Stirling engine," *Energy Conversion and Management*, vol. 165, pp. 447–458, 2018.

[26] R. Demko and L. Penswick, "Sage simulation model for technology demonstration convertor by a step-by-step approach," in *3rd International Energy Conversion Engineering Conference*, p. 5538, San Francisco, California, August 2006.

[27] K. Mahkamov and D. Djumanov, "Three-dimensional CFD modeling of a Stirling engine," in *Proceedings of the 11th International Stirling Engine Conference*, pp. 97–107, Rome, 2003.

[28] M. B. Ibrahim, Z.-G. Zhang, R. C. Tew Jr., D. Gedeon, and T. W. Simon, "CFD modeling of free-piston Stirling engines," in *36th Intersociety Energy Conversion Engineering Conference*, Savannah, Georgia, 2001.

[29] S. Wilson, R. Dyson, R. Tew, and M. Ibrahim, "Multi-D CFD modeling of free-piston Stirling convertor at NASA GRC," in *2nd International Energy Conversion Engineering Conference*, p. 5673, Providence, Rhode Island, August 2004.

[30] W. Jan and P. Marek, "Mathematical modeling of the Stirling engine," *Procedia Engineering*, vol. 157, pp. 349–356, 2016.

[31] N. Parlak, A. Wagner, M. Elsner, and H. S. Soyhan, "Thermodynamic analysis of a gamma type Stirling engine in non-ideal adiabatic conditions," *Renewable Energy*, vol. 34, no. 1, pp. 266–273, 2009.

[32] A. Sowale, E. J. Anthony, and A. J. Kolios, "Optimisation of a quasi-steady model of a free-piston Stirling engine," *Energies*, vol. 12, no. 1, p. 72, 2019.

[33] H. Li, X. Tian, L. Ge et al., "Development of a performance analysis model for free-piston Stirling power convertor in space nuclear reactor power systems," *Energies*, vol. 15, no. 3, p. 915, 2022.

[34] J. Sauer and H.-D. Kuehl, "Numerical model for Stirling cycle machines including a differential simulation of the appendix gap," *Applied Thermal Engineering*, vol. 111, pp. 819–833, 2017.

[35] D.-J. Kim and K. Sim, "Linear dynamic analysis of free-piston Stirling engines on operable charge pressure and working frequency along with experimental verifications," *Applied Sciences*, vol. 11, no. 11, p. 5205, 2021.

[36] G. F. C. Rogers and Y. R. Mayhew, *Engineering Thermodynamics*, Work and Heat Transfer, 1992.

[37] L. F. Moody, "Friction factors for pipe flow," *Transactions of the American Society of Mechanical Engineers*, vol. 66, no. 8, pp. 671–684, 1944.

[38] F. P. Incropera, D. P. DeWitt, T. L. Bergman, and A. S. Lavine, *Fundamentals of Heat and Mass Transfer*, Wiley, New York, 1996.

[39] C. J. Geankoplis, A. A. Hersel, and D. H. Lepek, *Transport Processes and Separation Process Principles*, Prentice Hall, Boston, MA, USA, 2018.

[40] W. M. Kays and A. L. London, *Compact heat exchangers*, Krieger Publishing Company, 1984.

[41] M. Tanaka, I. Yamashita, and F. Chisaka, "Flow and heat transfer characteristics of the Stirling engine regenerator in an oscillating flow," *JSME International Journal. Ser. 2, Fluids Engineering, Heat Transfer, Power, Combustion, Thermophysical Properties*, vol. 33, no. 2, pp. 283–289, 1990.

[42] J. G. Schreiber, S. M. Geng, and G. V. Lorenz, *RE-1000 Free-Piston Stirling Engine Sensitivity Test Results*, National Aeronautics and Space Administration Report, 1986.

[43] F. Formosa, "Coupled thermodynamic–dynamic semi-analytical model of free piston Stirling engines," *Energy Conversion and Management*, vol. 52, no. 5, pp. 2098–2109, 2011.

[44] Y.-C. Park, *Analysis and Verification with Quasi-Steady Flow Model Consideing Heat Transfer Characteristics of Stirling Engines*, Master, Seoul national university of science and technology, 2018.

[45] T. Muto and K. Nakane, "Unsteady flow in circular tube: velocity distribution of pulsating flow," *Bulletin of JSME*, vol. 23, no. 186, pp. 1990–1996, 1980.

[46] D. J. Shendage, S. B. Kedare, and S. L. Bapat, "Investigations on performance of Stirling engine regenerator matrix," in *Proceedings of the ASME/JSME 2011 8th Thermal Engineering Joint Conference. ASME/JSME 2011 8th Thermal Engineering Joint Conference*, Honolulu, Hawaii, USA, March 2011.

[47] D.-J. Kim, J.-S. Park, and K. Sim, "Development and performance measurements of a 2.5 kW-class free-piston Stirling converter with detailed design and fabrication processes," *Energy Reports*, vol. 8, pp. 15011–15026, 2022.